Experimental characterization of the intragranular strain field in columnar ice during transient creep

F. Grennerat [a,*], M. Montagnat [a], O. Castelnau [b], P. Vacher [c], H. Moulinec [d], P. Suquet [d], P. Duval [a]

[a] *LGGE UMR 5183, CNRS/UJF – Grenoble 1, Saint-Martin d'Hères, France*
[b] *Procédés et Ingénierie en Mécanique et Matériaux, CNRS, Arts & Métiers ParisTech, 151 Bd de l'hopital, 75013 Paris, France*
[c] *Laboratoire SYMME, Université de Savoie, domaine Universitaire BP 80439, 74944 Annecy le Vieux Cedex, France*
[d] *Laboratoire de Mécanique et Acoustique, 31, chemin Joseph Aiguier, 13402 Marseille Cedex 20, France*

Abstract

A digital image correlation (DIC) technique has been adapted to polycrystalline ice specimens in order to characterize the development of strain heterogeneities at an intragranular scale during transient creep deformation (compression tests). Specimens exhibit a columnar microstructure so that plastic deformation is essentially two-dimensional, with few in-depth gradients, and therefore surface DIC analyses are representative of the whole specimen volume. Local misorientations at the intragranular scale were also extracted from microstructure analyses carried out with an automatic texture analyzer before and after deformation. Highly localized strain patterns are evidenced by the DIC technique. Local equivalent strain can reach values as much as an order of magnitude larger than the macroscopic average. The structure of the strain pattern does not evolve with strain in the transient creep regime. Almost no correlation between the measured local strain and the Schmid factor of the slip plane of the underlying grain is observed, highlighting the importance of the mechanical interactions between neighboring grains resulting from the very large viscoplastic anisotropy of ice crystals. Finally, the experimental microstructure was introduced in a full-field fast Fourier transform polycrystal model; simulated strain fields are a good match with experimental ones.

1. Introduction

The deformation of polycrystalline materials gives rise to the build-up of heterogeneous stress and strain fields inside individual grains (*intra*granular scale), but also between adjacent grains (*inter*granular scale). These field heterogeneities originate from the anisotropic mechanical behavior of individual grains, which is responsible for complex mechanical interactions between adjacent grains upon macroscopic specimen loading. They have a large influence on the overall material response, as illustrated, for example, by Brenner et al. [1] for the yield stress of elastoplastic polycrystals.

The development of stress and strain heterogeneities has been studied in a number of papers by making use of full-field numerical approaches [2–7]. It has been observed that field heterogeneities increase quickly with the anisotropy of the local constitutive relation. A similar dependence to the non-linearity is expected, i.e. heterogeneities blow up when the local behavior becomes strongly non-linear [8]. It should also be mentioned that these trends are recovered by mean-field models based on homogenization theories [9].

On the experimental side, local strain can be characterized by means of digital image correlation (DIC) techniques. The method is based on the acquisition of successive images

of the specimen surfaces at different strain increments. The comparison of these images allows the identification of the displacement field at the specimen surface, which can be then derived to obtain the strain field of interest. This has been the subject of several studies on different metallic alloys exhibiting equiaxed and small (i.e. micrometer range) grains [10–12], in which the systematic development of localization bands at about 45° from the tensile angle and extending along several grain sizes has been observed. In these studies, the interpretation of strain localization is limited by the unknown microstructure of grains underneath the specimen free surface [11,13]. The application of DIC to geomaterials has so far been carried out on argillaceous rock [14], soft rock [15] and marble [16].

In this work, the DIC technique is applied to polycrystalline ice. This material exhibits a number of specific characteristics that can be used advantageously to gain an understanding of polycrystal behavior:

- Large specimens exhibiting columnar microstructures with centimetric grain size can be elaborated. Due to the absence of through-thickness microstructure gradients, fields measured at the specimen surface are representative of the whole specimen volume.
- Ice single crystals exhibit a single easy slip plane for dislocations; the viscoplastic anisotropy is therefore huge at the grain scale. Unlike in most hexagonal materials, twinning is not an active deformation mode, leading to a relatively simple behavior. The grain response can thus be characterized by a single Schmid factor, compared to many more for cubic or hexagonal metals.

Consequently, since the complete specimen microstructure and main active slip systems are known, one can also anticipate an easier interpretation of results.

This work is focused on the evolution of strain localization during the transient creep regime, corresponding to an overall strain of less than 10^{-2}. In that regime, the progressive development of an internal stress field is at the origin of the severe decrease in strain rate [17,18]. Concerning geophysical applications, the transient creep of polycrystalline ice is of interest with regard to, for example, the behavior of ice shelves submitted to ocean tides [19,20] and the production of heat within icy satellites [21,22].

This paper is organized as follows. Section 2 is devoted to the description of the specimen elaboration technique and obtained columnar microstructures. In Section 3, adaptation of the DIC technique to our sample configuration is described. The experimental resolution is estimated for the displacement and strain fields. The main results in terms of macroscopic strain and strain field evolution are given in Section 4. Specific results that can be inferred from these columnar microstructure are discussed in Section 5. The relation between local strain and local grain orientation is also analyzed. Results are also compared to predictions obtained by full-field modeling, based on the fast Fourier transform (FFT) approach of Moulinec and Suquet [23].

2. Columnar ice specimens

2.1. Ice behavior

Ice exhibits a hexagonal crystal structure. The elastic anisotropy of ice single crystals is small, the Young's modulus E varying by about 30%, depending on the direction of the loading axis with respect to the **c** axis. The highest value is along the **c** axis with $E = 11.8$ GPa at -16 °C [24].

The single crystals deform plastically essentially by glide of dislocations on the basal plane. There are three equivalent $\langle 1\,\bar{2}\,1\,0 \rangle$ directions for the Burgers vector, but slip in the basal plane is almost isotropic owing to the small stress sensitivity $n = 2$ for basal slip. At similar strain rates, the equivalent stress requested for non-basal slip is about 60 times larger than for basal slip [25].

For ice polycrystals deformed under the laboratory conditions considered in this work (strain rate lower than $10^{-6}\,\mathrm{s}^{-1}$ and temperature higher than -15 °C), strain is essentially due to intracrystalline dislocation glide [25]. The transient creep regime is characterized by a strong directional hardening until the strain rate minimum is reached for an overall strain of $\sim 1\%$. This strain rate decrease can reach three orders of magnitude; it is associated with the development of a strong internal stress field [17,25,26]. In the secondary creep regime, isotropic polycrystals deform (at similar stress levels) ~ 100 times slower than a single crystal optimally oriented for basal slip. The corresponding stress sensitivity is close to 3. At strains larger than 1–2% (tertiary creep regime), dynamic recrystallization is predominant, and new grain microstructures and crystal orientations are generated [27–30]. For a review on ice behavior, see Duval et al. [31].

2.2. Elaboration of columnar ice

Samples are made from distilled water slowly frozen under a vertical temperature gradient. The cold room is kept at 0 °C, while the negative temperature of the recipient bottom is adjustable. The water is constantly stirred by a motorized system to avoid the formation of air bubbles in the growing ice. The growth rate of solid ice, controlled with the temperature gradient, determines the final grain size: a faster growth rate produces smaller grains. In order to obtain columns with a nearly constant cross-section, it was necessary to gradually decrease the table temperature from -10 °C to -15 °C during the freezing process. An ice layer of 60 mm thickness was grown within about 9 h. Columnar specimens with nearly parallel (±15°) grain columns was thus obtained (Fig. 1). The chosen mean grain size (~ 7 mm) is a good compromise in order to: (i) obtain nearly parallel grain columns; (ii) get a sample thickness of only one grain; (iii) reach a reasonable intragranular
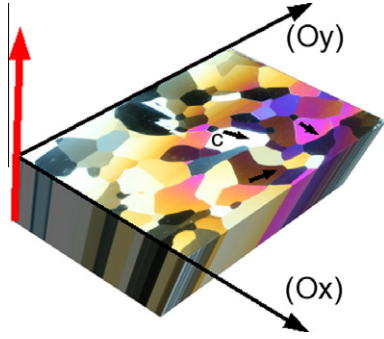
Fig. 1. Elaboration of columnar ice under a vertical temperature gradient. The red arrow indicates the direction of ice growth, which follows this gradient.

resolution with the DIC technique; and (iv) get enough grains in the whole specimen so that the sample size possibly approaches that of a representative volume element (RVE).

2.3. Microstructure characterization

Thin sections ($\sim$0.25 mm thickness) of the specimen are cut before and after deformation to characterize the microstructure with an automatic ice texture analyzer [32]. This is an optical system using polarized light that provides a map of c-axis orientations with a spatial resolution of 43 µm and an angular precision of 1°. In the thin section coordinate system (Oxyz), **c** is given by coordinates ($\sin \phi \cos \theta$, -$\sin \phi \sin \theta$, $\cos \phi$), with θ the azimuth and ϕ the colatitude. From these orientation data, size and spatial distribution of grains can be obtained. Most of the results presented here are extracted from a sample containing 243 grains, with a mean grain size of 5.7 mm. Its microstructure is shown in Fig. 2. The sample crystallographic texture is partly provided by the {0 0 0 2} pole figure (see Fig. 3). Most of the c-axes lie close to the sample surface plane: the average and standard deviation of the colatitude are 89.8° and 29.8°, respectively. One can therefore anticipate that plastic strain will occur essentially within the XY plane.
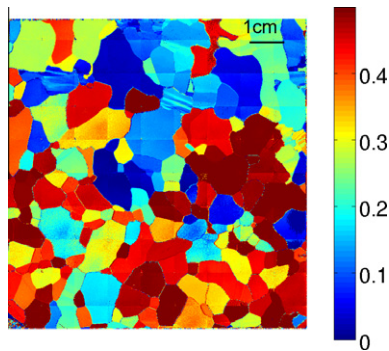

Fig. 2. Specimen microstructure measured with the automatic texture analyzer, before deformation. The color scale indicates the Schmid factors that have been calculated from the c-axis orientation data. On this map, the squared pattern of 1 cm size is an artefact from the analyzer.
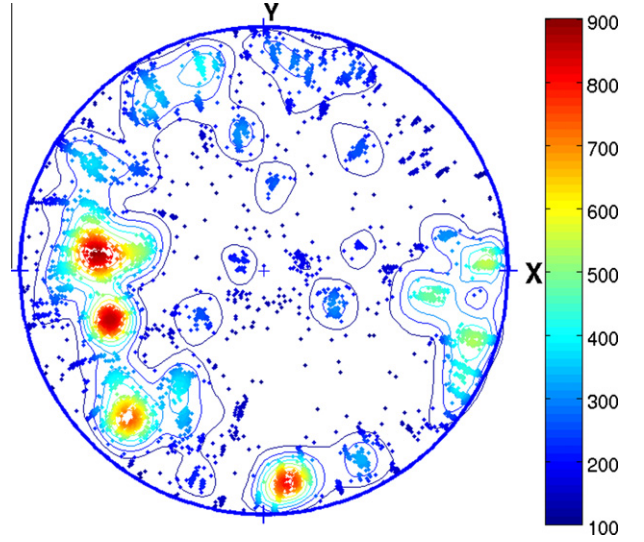

Fig. 3. Pole figure of the c-axes, before specimen deformation. Data points coming from the texture analyzer are indicated by dots. The color code indicates the pole figure intensity (arbitrary units). Y corresponds to the macroscopic compression direction.

As already discussed, grain orientation can be advantageously characterized by a single Schmid factor m_s. For uniaxial compression along direction Y, it reads

$$m_s = \sin \phi \sin \theta (1 - \sin^2 \phi \sin^2 \theta)^{1/2} \qquad (1)$$

Hereafter, m_s will be used only as a convenient geometrical criterion for characterizing grain orientation; it will not be associated with any assumption on stress uniformity within grains, which is not expected here. A large Schmid factor (=0.5) corresponds to a c-axis at 45° from the macroscopic compression direction; it vanishes for c-axes either parallel or perpendicular to that direction. Schmid factor values are superimposed on the initial specimen microstructure in Fig. 2. Uniform values within grains reveal the very small intragranular misorientation, smaller than the detection limit of the texture analyzer.

2.4. Mechanical tests

Uniaxial compression creep tests are performed in a cold room at -12 ± 1 °C under a constant stress of 0.5 MPa and for $\sim$50 h, to reach $\sim$1% overall strain (Fig. 4). Such a maximum strain level was chosen to stop the test in the secondary creep regime, just before the tertiary creep dominated by dynamic recrystallization. Samples are machined in the laboratory with high geometrical accuracy to a parallelepipedic shape of dimensions close to 90 mm $\times$ 90 mm $\times$ 15 mm (height $\times$ width $\times$ thickness). Two Teflon sheets are placed between the sample and the press in order to avoid friction at the specimen contact surfaces. It has been verified, on a specimen with very fine grains and exhibiting isotropic behavior (randomly oriented and equiaxed grains), that load is applied uniformly on the specimen surface, with no friction, since in that case the
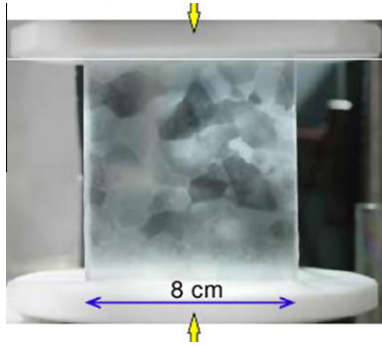
Fig. 4. Set-up for uniaxial compression tests. Individual grains can be detected thanks to cross polarizers.

Fig. 5. Typical speckle pattern (left) and zoom of a 20×20 pixels window (right).

displacement field measured by DIC is linear with x and y, as expected for homogeneous specimens [33]. The other surfaces of the sample are stress free.

The overall deformation of the sample along the compression direction Y is measured with a low-voltage displacement transducer (LVDT), positioned to record the whole specimen length changes.

2.5. Superimposition of strain and microstructure maps

In order to superimpose the strain fields obtained by the DIC technique with the specimen microstructure, two holes ($\phi = 1$ mm) are drilled in the sample next to its corners, before sampling the initial thin section. This enables a superimposition with a maximum error of a few pixels, i.e. ~0.2 mm. However, as discussed below, this accuracy is limited in practice by the inclination of grain boundaries that are not exactly parallel to the Z axis, and by the ice total thickness required for thin section elaboration (~2 mm). Based on these uncertainties, we estimate that the superimposition of strain and microstructure maps is accurate to within ~0.5 mm.

3. DIC set-up and resolution

The DIC technique relies on three steps: (i) speckle patterns are applied to the sample surface; (ii) successive images of the speckle pattern are taken along the deformation of the sample; and (iii) correlation between successive images is performed to measure surface displacements. The displacement resolution depends on these three steps, i.e. the quality of the speckle, the optical set-up and the correlation procedure. In the present study, use was made of the software 7D described in Ref. [34]. Technical details about the optical set-up are given in Appendix A.

3.1. Speckle deposition and characterization

Speckle deposition on ice is an issue for two reasons. First, use of toxic products is not allowed in cold rooms, and most of the regular substances used to create speckle patterns (paint, ink, etc.) do not adhere to the ice surface.
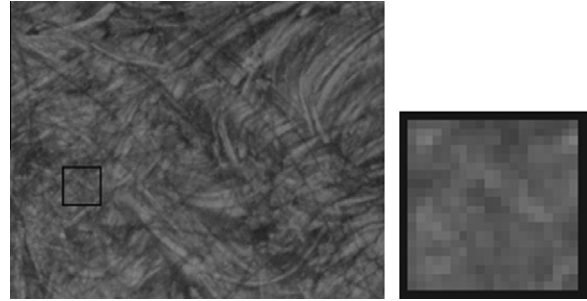
Second, the ice surface sublimates rapidly in the cold room at $-12\,°C$. After several attempts, the best solution was obtained by applying a small layer of shoe polish, after having polished the ice surface slightly with sandpaper to improve the cohesion of the speckle. A typical example of speckle pattern is shown in Fig. 5. The texture parameters of the speckle were studied following Refs. [35,36]. The mean standard deviation of the speckle of Fig. 5 is $\sigma \approx 22.5$ gray levels. This value has to be large enough to improve the subpixel resolution of the displacement in the DIC measurements; if $\sigma > 6$ gray levels, then a resolution of 0.01 pixels [36] can be reached. The autocorrelation radius of the speckle, which provides an average feature size [36], is obtained by averaging, in every direction, the length at half the maximum of the correlation. For most of our samples, the values were found to be between 3.7 and 7.4 pixels. From Ref. [35], the optimal value is between 3 and 5 pixels. Therefore, for the highest values of the radius, our speckle pattern is oversampled and a larger subset size will be required during matching. In these conditions, the spatial resolution that is achievable is slightly reduced.

3.2. DIC resolution

A virtual grid is associated with the initial image with a step of $n \times n$ pixels, and at each grid node a correlation window (also called the pattern size) of size $p \times p$ pixels is defined. In each correlation window, interpolation of gray levels enable the estimation of displacements with a subpixel (ideally 0.01 pixels) accuracy [35,37]. Here, a bilinear interpolation of the gray levels was used. The resulting displacement field is interpolated with a bilinear form on each element of the grid, and differentiated by a finite difference scheme to obtain the strain field.

Compromises have to be made with regard to the sizes of n and p. The size of the correlation window p determines the spatial resolution, which must be adapted to the actual strain heterogeneities to be characterized. p should be large enough to keep significant gray level gradients in the correlation window. The best spatial resolution that can be achieved is associated with the correlation radius r and the standard deviation of the speckle [35,36]. On the other hand, the smaller the step grid n, the worse the strain resolution. Here, values $p = n = 20$ pixels were selected. This

corresponds to a spatial resolution of 1.2 mm, i.e. small enough compared to the grain size to reach intragranular resolution.

Resolution of the DIC set-up depends on many factors. Effect of the overall image noise has been estimated by correlating many (∼10) images acquired successively without any specimen motion or set-up change. Unlike the no-motion theoretical result, the DIC technique identifies slight (artificial) specimen deformations. The mean standard deviation measured for component ε_{yy} was 0.16%.

In an attempt to evaluate systematic errors associated with subpixel displacements (the so-called "S curve"), the method proposed by Louche et al. [38] was used. Successive images of the fixed specimen were taken for small camera translations along the optical axis. Application of DIC to the set of images should lead to a purely radial displacement field. with an increasing amplitude from the image center to the edges. DIC subpixel errors can be estimated as the difference from this theoretical solution. Unfortunately, the camera motion generated caused unavoidable slight camera rotations, and the obtained translation field was not perfectly radial. However, an upper bound of ∼0.07 pixels could be determined for subpixel errors [33].

Out-of-plane specimen motion is another source of error for two-dimensional (2-D) DIC set-ups. This effect was estimated by applying a stereocorrelation technique [39] to a specimen exhibiting a microstructure similar to the one presented here. The out-of-plane motion could be estimated by the use of a second camera at an angle from the first one [40]. Although this set-up introduces important additional issues due to light reflection and pixel saturation, it could be confirmed that, after deformation, the sample surface was slightly wavy, though with wavelengths of the same order as the specimen size. The standard deviation of the out-of-plane displacement was $\sigma_z = 0.15$ mm over the whole surface. This value must be compared with the distance between the camera lens and the sample surface (900 mm) to estimate the associated deformation error, the standard deviation of which is then ∼0.017% (=0.15/900).

4. Results

4.1. Strain response

The overall specimen response under compressive creep loading is shown in Fig. 6. The average axial deformation based on DIC measurements is obtained from the relative displacement between the top and bottom parts of the specimen. There is a good match with strain measurements obtained by the LVDT; the slight discrepancy is probably due to the fact that the LVDT is not centered on the loading axis. For this specimen, the secondary creep regime is reached after ∼70 h for an axial strain of ∼−1%.

The evolution of strain heterogeneities measured by DIC is presented in Fig. 7. Maps of local equivalent strain obtained after −0.32%, −0.62% and −0.85% macroscopic
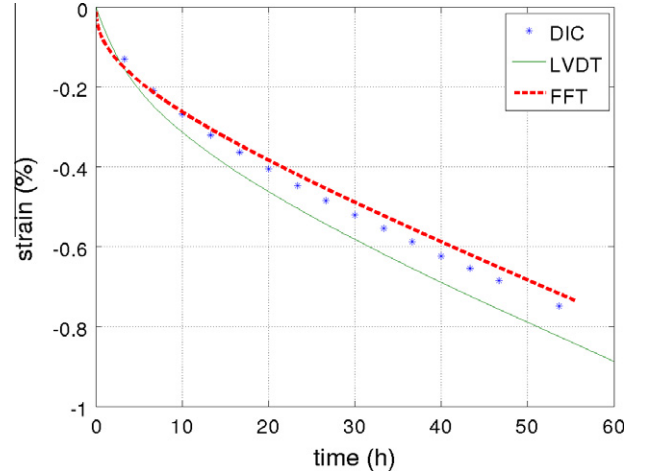

Fig. 6. Overall specimen response. The DIC contour average is compared with LVDT measurements and with the prediction from the FFT modeling (see Section 5.2).

axial strain are shown. Here, the equivalent strain is defined as $\varepsilon_{eq} = \sqrt{\frac{2}{3}\left(\varepsilon_{xx}^2 + \varepsilon_{yy}^2 + 2\varepsilon_{xy}^2\right)}$. This definition does not account for the components ε_{xz}, ε_{yz}, and ε_{zz}, which were not measured with our set-up, though they are expected to remain very small compared to ε_{xx}, ε_{yy}, and ε_{xy} due to the particular orientation of the grain's c-axis (it has been confirmed that the effective strain $\bar{\varepsilon}_{zz}$ is only about 15% of the value of $\bar{\varepsilon}_{yy}$ indicating that, at least macroscopically, the out-of-plane strain remains small). The deformation tends to concentrate into bands inclined with respect to the applied stress direction, the width of which is less than the grain size. This deformation pattern appears at an early stage of deformation, and does not evolve significantly with strain. For the three deformation stages shown in Fig. 7, local strain values reach up to 10 times the macroscopic average. Recalling that the strain evaluated by DIC is an average over n pixels (here ≈1.2 mm), very local strain values in the ice could be much larger than measured here.

Strain statistics, calculated over the whole specimen, can be inferred from these data. As shown in Fig. 8, computed for $\bar{\varepsilon}_{yy} = -0.85\%$, local strain values are spread over a large range. The equivalent strain is very well fitted by a log–normal distribution with a long tail at high strain, highlighting again the strong strain localization. Such a distribution appears during the early stage of the transient creep test. Interestingly, the distribution of the axial component ε_{yy} shows a significant positive part, even though the average value $\bar{\varepsilon}_{yy}$ is negative; local tensile strain arises in the specimen compressed at the macroscopic scale. A similar conclusion can be drawn for component ε_{xx}. The shear component distribution ε_{xy} is approximately symmetrical, and slightly narrower than the axial components.

To characterize the statistical orientation of localization bands at the specimen scale, the covariance of the strain field was calculated, following Ref. [41]. For this, we made use of the normalized correlation function
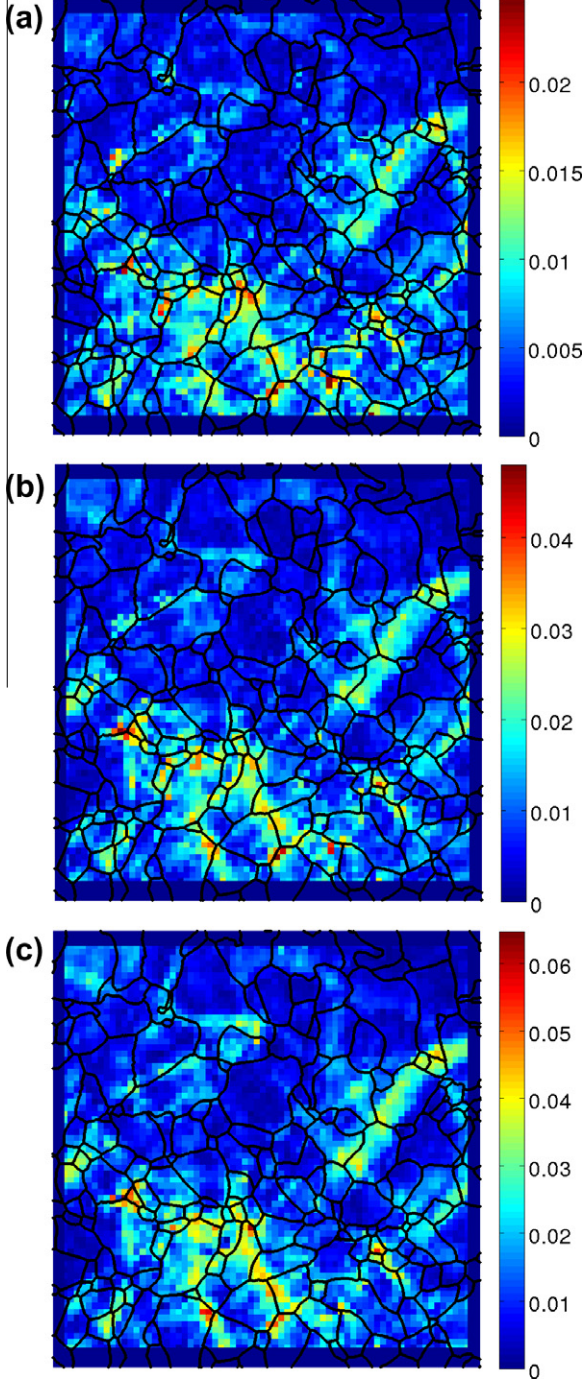
Fig. 7. Evolution of the equivalent strain in the transient creep regime, for an axial macroscopic deformation of (a) −0.32%, (b) −0.62% and (c) −0.85%. Note that the color scales are different. DIC could not be performed up to the edges of the specimen; the total specimen size corresponds to the outer blue square.

$$C(\mathbf{h}) = \frac{\int_S \varepsilon_{eq}(\mathbf{x})\varepsilon_{eq}(\mathbf{x} + \mathbf{h})dS}{\int_S \varepsilon_{eq}^2(\mathbf{x})dS} \qquad (2)$$

with S the considered surface, and $\mathbf{x}$ and $\mathbf{h}$ two position vectors. This relation requires periodicity of the strain map and no correlation of strain for distances larger than the image size. To perform the calculations, strain maps have been
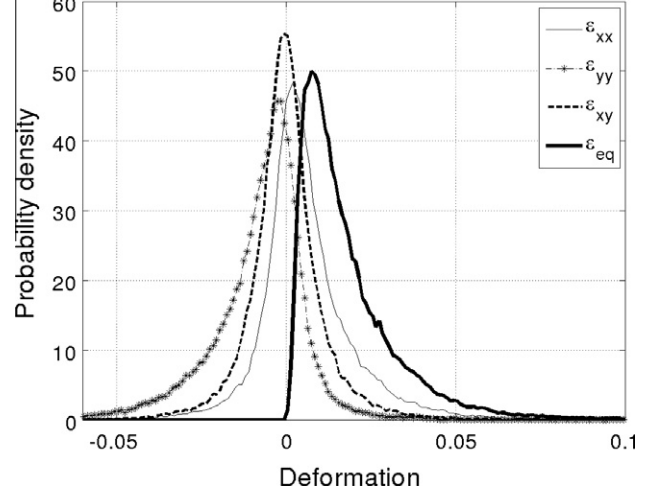

Fig. 8. Probability density of the different components of the deformation obtained at −0.85% macroscopic strain.
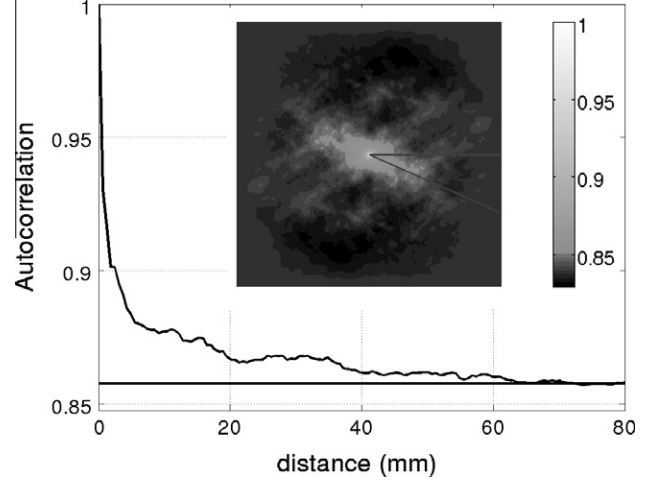

Fig. 9. (map) Covariogram of the equivalent strain presented in Fig. 7c, and (curve) profile of the covariogram for the direction $\chi = -32°$, corresponding to the largest correlation radius.

padded with their mean value, so that the considered surface S is a square of length twice the largest dimension of the specimen surface. The covariogram obtained for −0.85% overall strain is presented in Fig. 9, where the correlation function has been calculated for several directions of $\mathbf{h}$. We denote by χ the angle between $\mathbf{h}$ and the sample direction X, and $C_\chi(\mathbf{h})$ is the corresponding correlation function. A correlation radius r_χ is then defined as:

$$r_\chi = \text{Min}\left\{r \geqslant 0 | C_\chi(r) \leqslant C_\chi^\infty\right\} \qquad (3)$$

with C_χ^∞ the asymptotic value of C_χ at large $|\mathbf{h}|$. The major orientation of localization bands, denoted χ_{max}, corresponds to the value χ for which r_χ is maximum. A value of about −32° was found for the present specimen. This orientation does not evolve with strain, in agreement with the stable position of localization bands. It is worth noting that the correlation radius r_χ reaches values up to ~60 mm,

even at the beginning of the deformation test. This correlation radius provides a measure of the interaction length between the deforming grains, which is thus much larger (by about one order of magnitude) than the mean grain size. Note that it is also very close to the sample's dimensions (this point is discussed in Section 5). A similar analysis was performed on five other samples, revealing band orientations ranging between 30° and 60°, and interaction lengths from 8 to 12 times the mean grain size.

4.2. Link with the microstructure

The superimposition of strain maps with the specimen microstructure was performed using the procedure described in Section 2.5. Grain boundaries are indicated in Fig. 7. It can be observed that large localizations are most often encountered next to grain boundaries. Note, however, that this feature is not systematic: large strain can also be observed inside grains, and not all grain boundaries support a localization band. For a more quantitative analysis of the spatial repartition of strain, we took advantage of the actual specific columnar microstructure, in which all grain boundaries are nearly perpendicular to the specimen surface. A distance function providing the distance of any pixel to its nearest grain boundary can thus be defined without ambiguity. The results are shown in Fig. 10, in which, to improve the statistical relevance, we stacked data obtained for five different specimens with similar grain size. The figure clearly shows that strain is more heterogeneous next to grain boundaries than within grain interiors. Large strains are observed only in the vicinity of grain boundaries; however, pixels next to grain boundaries do not necessarily experience a strain larger than grain interiors. Moreover, on average, strain is probably slightly larger next to grain boundaries, though this tendency is fairly weak (red least-squares line on the figure).
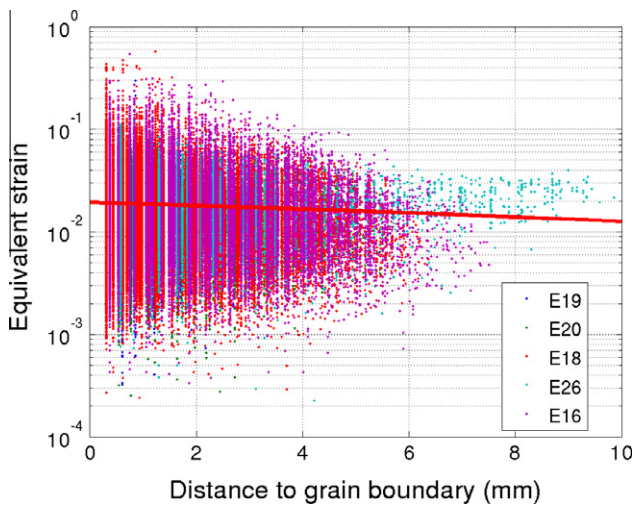
Finally, it is of interest to investigate the relation between the normalized equivalent strain $\varepsilon_{eq}/\bar{\varepsilon}_{eq}$ and the Schmid factor m_s. Recall that ice grains exhibit a single isotropic easy glide slip plane, and therefore the Schmid factor can be unambiguously determined for each grain. For doing this, pixels close to grain boundaries (distance < 0.3 mm) have to be discarded since it cannot be determined to which side of the grain boundary they belong, due to the uncertainties described in Section 2.5. Results, normalized by the overall equivalent strain, are presented in Fig. 11. Surprisingly, unlike the expected trend with ε_{eq} rapidly increasing with m_s, data do not show any specific tendency. A least-squares regression analysis of these data indicates that the deformation of grain increases slightly with the Schmid factor, although the correlation coefficient is rather small (<0.2) due to the large spread of data points. To improve the statistical relevance of this result, a similar analysis was performed on five other specimens exhibiting a qualitatively similar microstructure, and a very similar trend as in Fig. 11 was obtained. The important conclusion is that local grain deformation is not driven by the local Schmid factor. Grains with a large Schmid factor, generally considered as "soft" and "well oriented" for glide, do not tend to deform any more than grains with a small Schmid factor. Deformation data for a given value of Schmid tensor also show great variability.

5. Discussion

5.1. Strain distribution

In this experimental study, we adapted the DIC technique to investigate the mechanical response of ice at an intragran-

Fig. 10. Equivalent strain $vs.$ distance to grain boundaries for a set of five different samples with similar grain size. Each point corresponds to a pixel of the DIC images. The overall strain is ~0.8%.
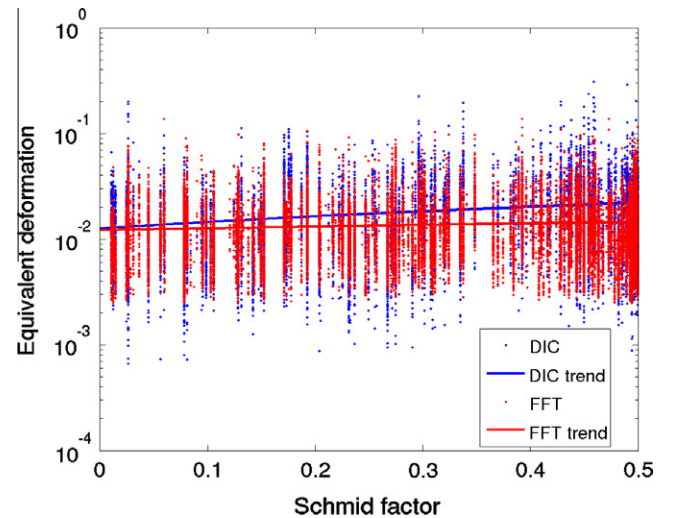
Fig. 11. Equivalent strain vs. Schmid factor for a macroscopic strain of ~-0.7%, as obtained by DIC and compared to FFT predictions (see Section 5.2).

ular spatial scale, and its evolution during deformation under uniaxial creep. The deposited speckle pattern was optimized so that the whole DIC set-up could reach adequate strain and spatial accuracies, which have been evaluated. We took advantage of some unique specificities of this material, namely: (i) the possibility of easy elaboration of columnar microstructures with no in-depth gradients and (ii) the deformation mechanisms with a single easy glide slip system, which is, moreover, almost isotropic. The distribution of strain was investigated in relation with the underlying grain microstructure. Huge strain heterogeneities were seen. Local equivalent strain measured by DIC reaches values as much as an order of magnitude larger than the macroscopic average. Recall, however, that strain values measured by the DIC technique are spatial average data, here over ~1.2 mm, and therefore the real (local) strain localization is expected to be larger. Thanks to the specific columnar microstructure, the distance of any point within a grain to the nearest grain boundary could be calculated. It was found that grain boundary regions, where the largest strain values are measured, deform in a much more heterogeneous way than grain interiors. Thanks to the specific dislocation slip systems, the Schmid factors of grains could also be calculated with no ambiguity. It was found that apparently "favorably oriented" grains (i.e. those with a high Schmid factor) do not necessarily deform any more than any other grains. We also stress that very similar results were obtained for many specimens, and therefore these results are not specific to the particular sample presented here.

Observations of the intragranular deformation of ice were presented in Refs. [42–45] for 2-D microstructures, some of them including ellipsoidal inclusions. The DIC technique was not applied at that time and strain heterogeneities were characterized indirectly through lattice misorientation measurements. Our experimental study suggests that stress is strongly redistributed throughout the entire specimen during creep loading. The observed strain localization must be associated with strong stress concentrations, with an ultimately minor role being played by local Schmid factors, but a strong impact from the neighborhood relationship. The creep behavior of isotropic polycrystalline ice has already been well documented in Ref. [17,26]. In the present work, due to the specific orientation of the **c**-axes lying almost parallel to the specimen surface, the measured strain rate obtained for the secondary creep (i.e. for $\bar{\varepsilon}_{eq} \sim 1\%$) is about 3–8×10^{-8} s^{-1}, in good agreement with what was measured by Plé [46] in similar conditions, and one order of magnitude larger than for isotropic ice with a random grain orientation [27]. At the very early stage of loading, the instantaneous specimen response is purely elastic. Since the elastic behavior of ice single crystals is close to isotropic, uniform stress and strain fields are thus expected. Unfortunately, the strain field could not be measured by DIC at very small overall strains (the elastic strain is $\sim 0.5 \times 10^{-4}$) due to the limited experimental resolution. As plastic deformation comes into play, with the activation of highly anisotropic dislocation glide almost

entirely on the basal slip system, stress must be redistributed. According to Refs. [25,17], as grain boundaries act as obstacles to basal slip, creep should relax the resolved stress on the basal plane on each grain and the load should be transferred to stiffer non-basal systems. Dislocation climb and cross-slip can also contribute to the relaxation of directional internal stresses. Transient creep is therefore associated with the development of a long-range internal stress field, responsible for the hardening associated with the large strain rate decrease. The hardening associated with primary creep is essentially kinematic, and is responsible for the large deformation recovered after unloading [25].

In the deformation maps obtained by DIC, it was observed that strain localization appears at an early stage of creep, i.e. for strain as small as -0.32%, with an already developed pattern of localization that does not evolve qualitatively with increasing strain. However, as shown in Ref. [26], the development of an internal stress field might be even more rapid; the stress heterogeneity associated with the high local viscoplastic anisotropy starts developing as soon as the plastic strain exceeds the elastic strain, and should be fully developed for deformation of the order of 5×10^{-4} [25,45].

An important result of this study is the relation between grain orientation and local strain. Surprisingly, local strain is only very poorly correlated with the Schmid factor of the unique easy glide slip plane. So-called "well oriented grains", i.e. those exhibiting a large Schmid factor, do not necessarily deform more than "badly oriented grains" (with a small Schmid factor). This is in contradiction to simple (intuitive) micromechanical models, such as the Reuss (or static) bound, assuming stress uniformity within the whole polycrystalline specimen [47], for which local deformation is entirely determined by the grain orientation. In ice, owing to the very high local viscoplastic anisotropy, the mechanical interaction between neighboring grains is very strong, and therefore the deformation of a specific grain is heavily influenced by its neighborhood [48,45]. Similar conclusions have been drawn for other highly anisotropic materials. In olivine, a mineral exhibiting only three independent easy glide slip systems, full-field numerical approaches show that a correlation is obtained between local equivalent stress (or strain rate) and grain orientation, but only when averaging is done over a very large number of grains exhibiting similar grain orientations but different neighborhoods [18,49]. The corollary of this feature is twofold. First, one must be very careful in interpreting the rheology of highly anisotropic polycrystals with very simple or *ad hoc* micromechanical models, such as the Reuss bound. Our results indicate that the activation of slip systems might be very different from such simple predictions. Second, for the interpretation of local observations of the polycrystal deformation, such as with transmission electron microscopy, one should consider the fact that the local stress might be very different from the macroscopic one.

The deformation pattern within the sample is characterized by localization bands, which are oriented between 30° and 60° from the compression axis. The length of the deformation bands is about an order of magnitude larger than the grain size, i.e. between 50 and 70 mm here, which is similar to the sample dimensions (about 90×90 mm^2). Therefore, we can expect local deformation mechanisms to interact over a distance much larger than the average grain size. This is consistent with the estimation of the spatial correlation length of dislocation avalanches being found to be much larger than the grain size [50]. As a consequence, the behavior is more or less independent of microscopic effects (grain size). The relation between the equivalent strain and the grain orientation is hidden, and only a small effect can be detected. The samples used in our experiments might not, however, constitute an RVE, so care must be taken when analyzing the results from a single isolated sample. In particular, the dispersion of the deformation pattern characteristics (band orientation and length) could be influenced by this sample size limitation and the particular boundary conditions applied here. A similar deformation band localization has been found both experimentally [51,41,52,11] and numerically [11,48]. In particular, Doumalin et al. [41] found similar deformation bands forming at an angle of ±52° with respect to the tensile direction in Zr, with the strain localization pattern having a characteristic length of 5–10 times the average grain size. Deformation band patterning during deformation of polycrystalline materials raises the problem of the determination of the RVE from only the observation of the microstructure [11]. Note, finally, that the estimated RVE length scale depends on the measurement resolution used for DIC experiments [13].

Our results indicate that the equivalent strain measured by DIC at different strain levels follows a log–normal distribution. In particular, a small volume fraction of grains deforms significantly more than the polycrystal average. From a computational approach, Moulinec and Suquet [53] highlight the influence of the non-linearity of the local behavior on the shape of the probability density of the strain fields in two-phase composites. In particular, a Gaussian distribution could be seen only with a linear behavior. Similarly, Lebensohn et al. [7] and Lee et al. [54] obtained assymetric distributions of stress and strain rates from an FFT full-field prediction in the case, respectively, of a viscous-linear aggregate and metal–metal composite materials. Using the same FFT approach, Castelnau et al. [18] predicted a strong increase in the distribution width with increasing local viscoplastic anisotropy of olivine grains. In particular, a bimodal shear stress distribution was obtained for an easy slip system of a theoretically "soft" crystal orientation; in many grains sharing the same crystal orientation, glide on the same easy slip plane can occur in opposite directions. Such observations clearly show the strong impact of neighboring grains on the local stress and strain conditions, the contribution of which increase with increasing anisotropy.

5.2. Comparison with full-field modeling

Full-field numerical simulations were performed using the FFT method initially proposed by Moulinec et al. [5,53], first applied to viscoplastic polycrystals by Lebensohn [6], and extended to elasto-viscoplastic composites using a step-by-step integration in time by Idiart et al. [8] (see also the numerical details in Ref. [55]). The FFT method consistsof finding a strain rate field associated with a kinematically admissible velocity field that minimizes the average local work rate under the compatibility and equilibrium constraints. An iterative scheme is used until convergence toward a fixed point. It is numerically more efficient than the finite element method [56], but is limited to microstructures submitted to periodic boundary conditions.

The specimen microstructure detailed in Section 2 was discretized into 1024×1024 Fourier points with a single layer of Fourier points in the third (Z) direction, assuming thus infinite column lengths. The experimental c-axis orientation was introduced in the model. The exact experimental boundary conditions (stress free lateral surface) could not be reproduced due to the periodicity constraint; therefore, fields predicted close to the specimen edges are not expected to be very accurate. With reard to the local constitutive relation, both the elastic and viscoplastic responses of ice crystals were considered [55]. Crystal plasticity accounts for three different families of slip systems, namely the basal, prismatic and $\langle a \rangle$-pyramidal systems, the latter two being taken stiffer than basal slip. A standard power law is considered for the slip rate $\dot{\gamma}^{(k)}$ on system (k):

$$\dot{\gamma}^{(k)} = \dot{\gamma}_0^{(k)} \left(\frac{|\tau^{(k)} - X^{(k)}|}{\tau_0^{(k)}} \right)^{n^{(k)}} \mathrm{sign}(\tau^{(k)} - X^{(k)}) \quad (4)$$

with τ^k the resolved shear stress acting on the system (k) and $\dot{\gamma}_0^{(k)}$ a reference slip rate, taken to be equal to 10^{-6} s^{-1}. The reference shear stresses τ_0 evolve following a Voce-type law:

$$\dot{\tau}_0^{(k)} = \left(\tau_{sta}^{(k)} - \tau_0^{(k)} \right)\dot{p}^{(k)}, \quad \dot{p}^{(k)} = \sum_{\ell=1}^{M} h^{(k,\ell)}|\dot{\gamma}^{(\ell)}| \quad (5)$$

where $h^{(k,l)}$ is a constant hardening matrix. X are back-stresses associated with kinematic hardening, given by a simple saturating law [57]:

$$\dot{X}^{(k)} = c^{(k)}\dot{\gamma}^{(k)} - d^{(k)}X^{(k)}|\dot{\gamma}^{(k)}| - e^{(k)}X^{(k)} \quad (6)$$

Parameters of this constitutive relation, which are slightly different from those used in Ref. [26], are provided in Table 1, together with $c = 9$ MPa, $d = 60$ and $e = 0.0003$ s^{-1}. Details about the identification procedure are published in Ref. [55].

As shown in Fig. 6, the model agrees well with the measured overall behavior despite a relatively rapid identification of the above parameters. The predicted strain and stress field after −0.84% macroscopic axial stress are presented in Fig. 12. It can be observed, by comparison with

Table 1
Initial (*ini*) and stationary (*sta*) values of the reference shear stresses $\tau^{(0)}$, stress sensitivity *n* and hardening matrix *H* (last three columns) (values of τ and *H* are given in MPa).

	τ_{ini}	τ_{sta}	n	H	Ba	Pr	Pyr
Ba	0.1	0.022	2	Ba	70	125	0
Pr	0.15	1.625	2.85	Pr	125	110	0
Pyr	3.875	3.875	4	Pyr	0	0	0

Fig. 7, that the general location and orientation of the deformation bands are well predicted, with strain concentration at triple junctions and close to grain boundaries, but also often within grain interiors. The largest predicted local strain is about 10 times the macroscopic equivalent strain, and appears to be localized in much finer areas than in the experimental observations. This discrepancy has to be associated with the different spatial resolutions, which is much lower for the DIC results. One cannot rule out the probable effects of periodic boundary conditions discussed above, especially since the sample size is quite small compared to the characteristic length of the strain localization pattern. Nevertheless, the overall good match between the localization pattern predicted by FFT and that mea-

sured experimentally tends to indicate that boundary conditions have a minor influence compared to the mechanical interaction between grains.

The large strain heterogeneity is associated with a high concentration of local stresses, as shown in Fig. 12 (down). With the actual FFT spatial resolution, the local equivalent stress, defined as $\sigma_{eq} = \sqrt{\frac{3}{2}\sigma_{ij}\sigma_{ij}}$, can reach up to five times the macroscopic one, but note that there is no one-to-one correspondence with the local equivalent strain. Small strain values can be associated with either large or small stress, depending on the considered location, in agreement with earlier findings on olivine polycrystals [58]. Sensitivity tests (not presented here) also showed that the resistance of hard prismatic and pyramidal slip systems, and their hardening, strongly influence the level of strain heterogeneity. The balance between isotropic and kinematic hardening should also play a role in the simulation of the transient creep kinematics toward secondary creep, and will have to be estimated carefully. A more detailed comparison between FFT full-field modeling and DIC results requires a broader study beyond the scope of the present paper. However, the good match already obtained shows that DIC experimental results are solid. In particular, as seen in Fig. 11, the lack of correlation between local equivalent strain and grain Schmid factor, observed experimentally, is fully reproduced by the FFT approach.

6. Summary and conclusions

The strain field was evaluated in ice polycrystals by a DIC technique with an intragranular spatial resolution. Sample microstructure was essentially 2-D, with columnar grains exhibiting *c*-axis orientation nearly parallel to the sample plane and little in-depth microstructure gradient, so that plane strain conditions could be approached. Samples were deformed under compression creep, and the strain field evolution was estimated all along the transient creep until about 1% macroscopic axial strain.

The measured strain field is highly heterogeneous, with local values up to an order of magnitude larger than the macroscopic strain. It was observed that tensile strains can take place locally in the macroscopically compressed specimen. The strain is more heterogeneous in the grain boundary regions than within the grain interiors. Strain heterogeneities tend to concentrate into bands, similar to observations for other materials [51,41,11]. The length of the bands is ∼8 times the average grain size. Therefore, local deformation mechanisms are expected to interact over a distance larger than the average grain size, and close to the actual sample dimension. Statistical measurements performed over several similar microstructures reveal no clear correlation between grain orientation and strain level. The present experimental results thus do not support the classical model opposing "well oriented" grains to "badly oriented" grains (depending on the local Schmid factor) to explain ice deformation. The strong viscoplastic anisotropy
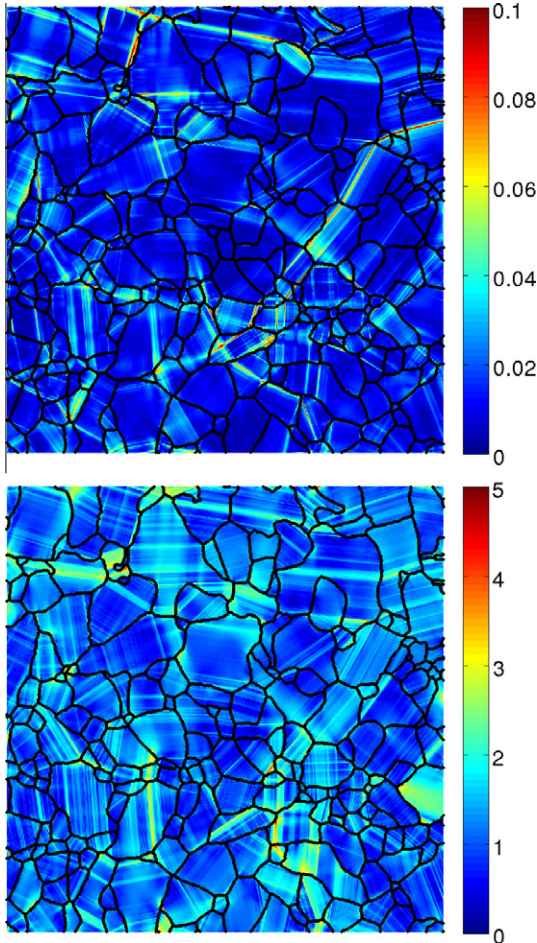

Fig. 12. Full-field FFT predictions for the distribution of (up) the equivalent strain and (down) the equivalent stress of a macroscopic axial deformation of −0.84%.

of ice induces strong mechanical interactions between neighboring grains that strongly influence local deformations. Observed strain heterogeneities are reproduced well by the elasto-viscoplastic full-field FFT model in which the experimental microstructure is introduced. In particular, the lack of correlation between local grain orientation and local equivalent strain supports experimental observations.

The experimental measurement of the intragranular strain field developing during transient creep appears to be a powerful tool for identifying and validating full-field elasto-viscoplastic approaches aimed at representing the material response during complex deformation path. In addition, microstructure evolutions, such as the local lattice misorientations associated with rapidly appearing kink bands, will be further analyzed with respect to local strain and stress fields.

Acknowledgements

Appendix A. DIC optical set-up

The surface of ice reflects light efficiently. To avoid sharp light reflections and the saturation of some of the pixels in the images, the entire device (sample plus press) was covered with a semi-transparent plastic film to scatter all light sources. The sample was illuminated with two lamps, each composed of several white LEDs, positioned about 20 cm away from the sample and behind the plastic film.

For image acquisition, a 21.1-megapixel (3750×5630 pixels) CMOS digital reflex camera (Canon EOS 5D Mark II) with a 180 mm f/3.5 macrolens was used. The lens to sample distance was 90 cm, the exposure time 0.6 s, the aperture number 10, the ISO value 500 and the focus set in the manual position to avoid any changes during the experiment. The camera was connected to a laptop computer, and images were recorded every 20 min. With this set-up, the pixel size of the correlated images was 0.06 mm.

The lens resolution is limited by diffraction features. Diffraction patterns are characterized by the Airy disc radius $r_{Airy} = 0.61 \frac{\lambda}{\alpha}$, where λ is the wavelength of the LED and α is the numerical aperture $\left(\alpha = \frac{D}{2f} = \frac{1}{2AV} \right)$. For a wavelength of 700 nm and an aperture value $AV = 10$, we obtain $r_{Airy} \approx 8.5 \mu m$, which is much smaller than the superpixel size ($\sim 60 \, \mu m$) as required.

References

[1] Brenner R, Lebensohn R, Castelnau O. Int J Solids Struct 2009;46:3018–26.

[2] Dawson PR, Beaudoin AJ. In: Kocks UF, Tomé CN, Wenk H, editors. Texture and anisotropy. preferred orientations in polycrystals and their effect on materials properties. Cambridge: Cambridge University Press; 1998. p. 297–305.

[3] Mika D, Dawson P. Acta Mater 1999;47(4):1355–69. http://dx.doi.org/10.1016/S1359-6454(98)00386-3.

[4] Barbe F, Forest S, Cailletaud G. Int J Plast 2001;17:537–63.

[5] Moulinec H, Suquet P. Comput Methods Appl Mech Eng 1998;157(1-2):69–94.

[6] Lebensohn RA. Acta Mater 2001;49(14):2723–37.

[7] Lebensohn R, Castelnau O, Brenner R, Gilormini P. Int J Solids Struct 2005;42(20):5441–59.

[8] Idiart MI, Moulinec H, Ponte Castañeda P, Suquet P. J Mech Phys Solids 2006;54:1029–63.

[9] Lebensohn R, Liu Y, Ponte Castañeda P. Proc Royal Soc Lond Ser A 2004;460(2045):1381–405.

[10] Raabe D, Sachtleber M, Zhao Z, Roters F, Zaefferer S. Acta Mater 2001;49(17):3433–41.

[11] Héripré E, Dexet M, Crépin J, Gélébart L, Roos A, Bornert M, et al. Int J Plast 2007;23(9):1512–39.

[12] Sutton M, Li N, Garcia D, Cornille N, Orteu J, McNeill S, et al. Exp Mech 2007;47:789–804. http://dx.doi.org/10.1007/s11340-007-9041-0.

[13] Efstathiou C, Sehitoglu H, Lambros J. Int J Plast 2010;26:93–106.

[14] Bornert M, Valès F, Gharbi H, Nguyen Minh D. Strain 2010;46(1):33–46.

[15] Nguyen T, Hall S, Vacher P, Viggiani G. Tectonophysics 2010;503(1–2):117–28.

[16] Xu L, Evans B. J Geophys Res 2010;115:B04202. http://dx.doi.org/10.1029/2009JB006458. 18p.

[17] Ashby MF, Duval P. Cold Reg Sci Technol 1985;11:285–300.

[18] Castelnau O, Blackman DK, Lebensohn RA, Ponte Castañeda P. J Geophys Res 2008;113:B09202. http://dx.doi.org/10.1029/2007JB005444.

[19] Jenkins A, Corr H, Nicholls K, Stewart G, Doake CSM. J Glaciol 2006;52(178):325–45.

[20] King MA, Makinson K, Gudmundsson GH. Geophys Res Lett 2011;38:L08501. http://dx.doi.org/10.1029/2011GL046680.

[21] Sotin C, Tobie G, Wahr J. In: Pappalardo RT, McKinnon WB, Khurana K, editors. Europa after Galileo. Tucson (AZ): The University of Arizona Press; 2009. p. 85–118.

[22] Han L, Showman AP. Icarus 2011;212(1):262–7.

[23] Moulinec H, Suquet P. CR Ser II Méc Phys Chim Astronom 1994;318(11):1417–23.

[24] Gammon PH, Kiefte H, Clouter MJ, Denner WW. J Glaciol 1983;29(103):433–60.

[25] Duval P, Ashby MF, Anderman I. J Phys Chem 1983;87(21):4066–74.

[26] Castelnau O, Duval P, Montagnat M, Brenner R. J Geophys Res 2008;113:B11203. http://dx.doi.org/10.1029/2008JB005751.

[27] Jacka TH, Maccagnan M. Cold Reg Sci Technol 1984;8:269–86.

[28] de La Chapelle S, Castelnau O, Lipenkov V, Duval P. J Geophys Res 1998;103(B3):5091–105.

[29] Duval P, Arnaud L, Brissaud O, Montagnat M, Chapelle SDL. Ann Glaciol 2000;30:83–7.

[30] Montagnat M, Duval P. Earth Planet Sci 2000;183:179–86.

[31] Duval P, Montagnat M, Grennerat F, Weiss J, Meyssonnier J, Philip A. J Glaciol 2010;56(200):1059–68.

[32] Russell-Head DS, Wilson C. J Glaciol 2001;24(90):117–30.

[33] Grennerat F. PhD thesis. Université de Grenoble; 2011.

[34] Vacher P, Dumoulin S, Morestin F, Mguil-Touchal S. Proc Instn Mech Engrs 1999;213:811–7.

[35] Sutton M, Orteu J, Schreier H. Image correlation for shape, motion and deformation measurements: basic concepts, theory and applications. New York: Springer; 2009.

[36] Triconnet K, Derrien K, Hild F, Baptiste D. Opt Lasers Eng 2009;47:728–37.

[37] Louche H, Bouabdallah K, Vacher P, Coudert T, Balland P. Exp Mech 2008;48:741–51.

[38] Yang DS, Bornert M, Gharbi H, Valli P, Wang LL. In: Brémand F, editor. EPJ web of conferences 6, vol. 6. ICEM 14 – 14th International Conference on Experimental Mechanics, Poitiers, France; 2010. id.22019.

[39] Robert L, Nazaret F, Cutard T, Orteu J-J. Exp Mech 2007;47:761–73. http://dx.doi.org/10.1007/s11340-007-9062-8.

[40] Coudert T. PhD thesis. Université de Savoie; 2005.

[41] Doumalin P, Bornert M, Crépin J. Méc Ind 2003;4:607–17.

[42] Mansuy P, Meyssonnier J, Philip A. Lect Notes Phys 1999;533:215–24.

[43] Mansuy P, Philip A, Meyssonnier J. Ann Glaciol 2000;30:121–6.

[44] Mansuy P, Meyssonnier J, Philip A. Comput Mater Sci 2002;25(1-):142–50.

[45] Montagnat M, Blackford JR, Piazolo S, Arnaud L, Lebensohn RA. Earth Planet Sci Lett 2011;305(1–2):153–60.

[46] Plé O. PhD thesis. Université Joseph Fourier-Grenoble I; 1998.

[47] Kocks UF, Tomé CN, Wenk H, editors. Texture and anisotropy. preferred orientations in polycrystals and their effect on materials properties. Cambridge: Cambridge University Press; 1998.

[48] Lebensohn R, Montagnat M, Mansuy P, Duval P, Meyssonnier J, Philip A. Acta Mater 2009;52(18):5347–61.

[49] Castelnau O, Lebensohn R, Brenner R, Rollett A. Acta Mater 2008;56(15):3914–26.

[50] Richeton T, Weiss J, Louchet F. Acta Mater 2005;53:4463–71.

[51] Delaire F, Raphanel JL, Rey C. Acta Mater 2000;48(5):1075–87.

[52] Gélébart L, Crépin J, Dexet M, Sauzay M, Roos A. J. ASTM Int 2004;1:JAI1233.

[53] Moulinec H, Suquet P. Eur J Mech A: Solids 2003;22(5):751–70.

[54] Lee S-B, Lebensohn R, Rollett A. Int J Plast 2011;27(5):707–27.

[55] Suquet P, Moulinec H, Castelnau O, Montagnat M, Lahellec N, Grennerat F, et al. Procedia IUTAM; 2011.

[56] Prakash A, Lebensohn R. Simul Mater Sci Eng 2009;17:1–16.

[57] Chaboche JL. Int J Plast 2008;24:1642–93.

[58] Castelnau O, Cordier P, Lebensohn RA, Merkel S, Raterron P. CR Phys 2010;11:304–15.